Chinese Journal of
POLYMER SCIENCE

RESEARCH ARTICLE

https://doi.org/10.1007/s10118-026-3805-4
Chinese J. Polym. Sci.

Cross-section Engineering of Melt-spun Poly(lactic acid)/Cesium Tungsten Bronze Fibers: Balancing Photothermal Conversion and Thermal Insulation

Peng-Cheng Zheng†, Jie-Rui Chen†, Ji-Guang Dong, Yan-Ning Mao, Hao Huang, and Jin-Chao Yu*

College of Textile and Clothing Engineering, Soochow University, Suzhou 215123, China

Abstract Photothermal conversion fibers enable active solar-thermal management for personal insulation. However, solid circular architectures suffer from high thermal conductivity, excessive specular gloss, and limited bulkiness. We report melt-spun poly(lactic acid) (PLA)/cesium tungsten bronze (Cs_xWO_3) composite fibers with systematically varied cross-sections: solid circular (F-circular), circular hollow (F-hollow), flat (F-flat), I-shaped (F-dumbbell), cross-shaped (F-cruciform), and penta-channel-shaped (F-penta-channel). The cross-sectional curvature and air-cavity content balance the photothermal conversion and thermal resistance while tuning the surface optical and capillary behavior. The F-circular fiber maximizes the near-infrared absorptance (0.72) and photothermal response (14.4 °C temperature rise under 600 $W{\cdot}m^{-2}$) because geometric isotropy minimizes interfacial scattering; conversely, it exhibits the lowest thermal insulation (ΔT=0.4 °C). Increasing the cross-sectional complexity progressively reduces light harvesting, as multi-ridge and flange structures amplify reflection losses at the fiber–air interface. At the same time, the F-cruciform fiber achieves the highest thermal insulation (ΔT=1.5 °C) through a four-fold symmetric air network that suppresses convective and conductive heat transfer. The shift from specular to diffuse reflection with increasing profile complexity reduces the dyeing depth (L^* increases from 58 to 72) but enhances the wicking capability (F-cruciform reaches 15.6 cm). Mechanical testing showed a positive correlation between circumferential symmetry and tensile strength; geometric discontinuities in the F-flat fiber reduced the tenacity to 3.01 $cN{\cdot}dtex^{-1}$, but all profiled fibers remained processable for weaving and heat setting. Thus, cross-sectional geometry functions as a decisive structural parameter for balancing photothermal, thermal insulation, and comfort properties in bio-based fibers, establishing design guidelines for lightweight, fur-like sustainable thermal textiles.

Keywords Poly(lactic acid) fiber; Photothermal conversion; Thermal insulation; Cross-section engineering; Melt spinning

Citation: Zheng, P. C.; Chen, J. R.; Dong, J. G.; Mao, Y. N.; Huang, H.; Yu, J. C. Cross-section engineering of melt-spun poly(lactic acid)/cesium tungsten bronze fibers: balancing photothermal conversion and thermal insulation. *Chinese J. Polym. Sci.* https://doi.org/10.1007/s10118-026-3805-4

INTRODUCTION

The global energy crisis and urgent carbon neutrality targets have prompted the textile industry to reduce fossil resource dependence and transition to bio-based materials.[1] The development of sustainable, high-performance thermal insulation fibers is essential for the high-value application of bio-based materials.[2] Photothermal conversion fibers directly harvest solar energy and convert it to heat without external electrical input, thereby enabling active heat generation.[3] This approach overcomes the bulkiness and reliance on static thermal resistance, which constrains conventional passive insulation materials.[4] Consequently, these fibers have attracted growing interest for personal thermal management applications.

Poly(lactic acid) (PLA), a representative biomass-derived polyester, combines biocompatibility, biodegradability, and a low-carbon footprint,[5,6] making it an attractive matrix for sustainable photothermal fibers. However, the intrinsic optical transparency of PLA results in poor light harvesting,[7] preventing effective photothermal conversion. Therefore, the incorporation of photothermal nanofillers into PLA is necessary to confer light-absorption capability. Thus, various photothermal fillers have been investigated. Noble metals (*e.g.*, Au[8] and Ag[9]) exhibit strong extinction coefficients and high photothermal conversion efficiencies in the visible (Vis) to near-infrared (NIR) region *via* localized surface plasmon resonance (LSPR). However, their high cost, susceptibility to oxidation at elevated temperatures, and tendency to induce polymer degradation during melt-spinning limit their practical use.[10] Carbon-based materials (graphene, carbon nanotubes, and carbon black) have been widely adopted because of their broadband absorption, yet their intrinsic deep black coloration restricts their use in light-colored thermal textiles.[2,11,12] Light-colored inorganic semiconductors such as indium tin oxide (ITO) and antimony-doped tin oxide (ATO) rely on carrier plasma resonance induced by heavy doping to

* Corresponding author, E-mail: jcyu@suda.edu.cn
† These authors contributed equally to this work.
Received May 26, 2026; Accepted July 5, 2026; Published online October 23, 2026

© Chinese Chemical Society
Institute of Chemistry, Chinese Academy of Sciences

generate optical responses in the NIR region while preserving visible-light transparency.[13,14] Nevertheless, their mechanism is dominated by plasmonic reflection and shielding rather than absorption, yielding lower photothermal absorption efficiencies compared with materials that rely on intrinsic light absorption.[15] In contrast, non-stoichiometric cesium tungsten bronze (Cs_xWO_3) functions *via* a synergistic mechanism of oxygen-vacancy-induced LSPR and polaron transitions, enabling high NIR absorption while maintaining a high visible-light transmittance.[16] This selective absorption of NIR light, combined with visible-light transmission, yields a transparent or pale blue appearance in the fibers.[17,18] Combined with the high photothermal conversion efficiency, excellent thermal stability during processing, and good compatibility with melt spinning, these properties render Cs_xWO_3 attractive for light-colored, eco-friendly photothermal fibers.[17,18] Our previous work showed that conventional circular PLA/Cs_xWO_3 composite fibers (0.4 wt%) raised fabric surface temperatures by 6.1 and 9.9 °C relative to PLA/ATO and neat PLA fabrics, respectively, after 10 min of xenon lamp irradiation (600 W·m^{-2}).[18] The pale blue intrinsic coloration was also compatible with subsequent dyeing processes.[18]

Although conventional circular PLA/Cs_xWO_3 fibers exhibit excellent photothermal conversion performance, their dense solid structure leads to a high thermal conductivity and insufficient bulkiness.[19,20] A smooth surface also generates excessive specular gloss and lacks the soft texture required for fur-like aesthetics and thermal insulation.[21] Cross-section engineering addresses these limitations by introducing micro- and nanoscale air cavities and modulating the interface curvature, thereby improving thermal insulation and surface texture simultaneously.[22,23] Beyond the thermal and tactile properties, the material morphology also governs the photothermal conversion efficiency. For example, bioinspired microstructures, such as hierarchical protrusions on Gaboon viper dorsal scales and wavy surfaces, can increase light absorption through light trapping.[24] In *Bitis rhinoceros*, these structures reduce reflectance to merely 10.8% in the UV-near-IR range, yielding a fourfold lower reflectance than pale scales.[24] However, their high specific surface areas and complex fabrication processes make it difficult to translate these designs directly into melt-spun microfibers. In contrast, tailoring the fiber cross-sectional geometry through profiled spinneret design offers a practical strategy that balances continuous large-scale production with optical performance optimization; the cross-sectional curvature directly modulates the optical path within the fiber.[25] Liu *et al*.[26] reported that double-cruciform and dumbbell-shaped polyester fibers achieve deep coloration through intense light scattering induced by complex cross-sections, indicating enhanced light absorption. Guo *et al*.[27] demonstrated that triangular cross sections significantly increased light reflectance (from 63.99% to 88.07%), enabling passive cooling with a 7.17 °C reduction in skin temperature. Although neither study addressed photothermal conversion directly, both demonstrated that cross-sectional geometry critically governs light propagation pathways, specifically the competition between absorption and reflection. Therefore, the underlying mechanism is complex and highly structure dependent.

Previous studies have largely focused on the influence of fiber cross-sections on individual optical functions, such as luster and color[26] or passive radiative cooling[27] without exploring the synergistic mechanism between photothermal conversion and thermal insulation. Hollow and profiled cross-sections can significantly reduce thermal conductivity and increase bulkiness by trapping static air, thereby enhancing thermal insulation.[28,29] However, the trade-off between this structural optimization and photothermal conversion efficiency is yet to be clarified.[4] For the PLA/Cs_xWO_3 composite fiber system, a systematic investigation of how cross-section engineering (*e.g.*, hollow structures, geometric shapes) balances light absorption and thermal resistance has not been established.[18]

In this work, we used Cs_xWO_3 as the photothermal functional filler and PLA as the matrix to prepare a series of profiled composite fibers (including hollow and non-circular cross sections) *via* melt spinning. We systematically investigated how the cross-sectional geometry simultaneously regulates photothermal conversion, thermal resistance, surface optical behavior, dyeing performance, and wicking behavior. This enables us to elucidate the structure–property relationships that connect profiled architectures to photothermal, thermal insulation, and comfort properties. These findings establish design guidelines for efficient, lightweight, and fur-like bio-based photothermal insulation fibers.

EXPERIMENTAL

Materials

Poly(lactic acid) (PLA, LX530, intrinsic viscosity 0.89 dL·g^{-1} measured in tetrahydrofuran at 30 °C) was supplied by TotalEnergies Corbion (Thailand). Cesium tungsten bronze (Cs_xWO_3) nanopowder (particle size <100 nm) was purchased from Hongwu Nano New Materials Co., Ltd., (China). Antioxidant 1010 (BASF SE, Germany) and hydrolysis stabilizer KSJ-100 (Shanghai Handian Technology Co., Ltd., China) were used as-received. All materials were used without further purification, unless otherwise stated.

Sample Preparation

Preparation of PLA/Cs_xWO_3 masterbatch

PLA pellets were cryogenically ground and sieved through a 35–40 mesh. The resulting powder was thoroughly dried and premixed with Cs_xWO_3 nanopowder using a high-speed mixer. The blend was melt compounded in a co-rotating twin-screw extruder at 168–178 °C. To suppress thermal oxidation and hydrolytic degradation of PLA during processing, 0.2 wt% antioxidant (1010) and 0.4 wt% hydrolysis stabilizer (KSJ-100) were incorporated. The extrudate was cooled in a water bath and pelletized to obtain a photothermal masterbatch containing 6 wt% Cs_xWO_3.

Preparation of PLA/Cs_xWO_3 profiled fibers

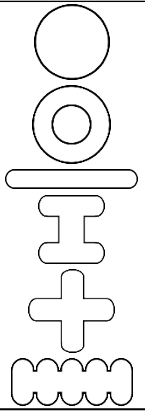
The PLA pellets and the masterbatch were dried in a dehumidifying hopper at 130 °C to a moisture content below 0.003 wt%. The fibers were produced using a laboratory-scale melt-spinning apparatus. The Cs_xWO_3 content in the final fibers was controlled to 0.4 wt% *via* masterbatch dilution. The spinning parameters were as follows: melt temperature, 210 °C; metering pump throughput, 15 mL·min^{-1}; 24-orifice spinneret; and take-

https://doi.org/10.1007/s10118-026-3805-4

up speed, 600 m·min^{-1}. The fibers were cooled in ambient air (about 26 °C) without forced side blowing air. The cooling length (spinneret-to-godet distance) was 0.9 m. Profiled fibers with different cross-sectional geometries were prepared by using spinnerets with circular, circular hollow, flat, dumbbell, cruciform, and penta-channel-shaped orifices.

The as-spun fibers were post-drawn using a two-stage hot-drawing unit consisting of a preheating roll at 60 °C and hot plate at 140 °C, with a total draw ratio of 4.0. The sample codes and corresponding cross-sectional morphologies are listed in Table 1.

Table 1 Sample codes and cross-sectional geometries of the prepared PLA/Cs_xWO_3 fibers.

Sample code	Cross-sectional geometries
F-circular	
F-hollow	
F-flat	
F-dumbbell	
F-cruciform	
F-penta-channel	

Fabric preparation

The profiled PLA/Cs_xWO_3 fibers were first combined on a high-speed winding machine and then twisted using a two-for-one twisting machine at a twist density of 150 twists·m^{-1} with an S-twist direction, yielding multifilament yarns with a linear density of approximately 520 dtex. These yarns were used as both warps and wefts to weave plain fabrics on a sample loom. The resulting fabrics had a warp density of 25 ends·cm^{-1}, weft density of 17 picks·cm^{-1}, and areal density of approximately 245 g·m^{-2}.

Characterization

Morphological characterization

The surface and cross-sectional morphologies of the fibers were examined using field-emission scanning electron microscopy (FE-SEM; Hitachi S-4800). Cross-sectional specimens with a section thickness of approximately 20 μm were prepared using a Hardy microtome. All the samples were sputter-coated with a gold layer (about 10 nm) prior to imaging to enhance the electrical conductivity.

Geometric specific surface area

The cross-sectional perimeter (C) of the fibers was extracted from the SEM images using an image-processing software (Adobe Photoshop). The geometric specific surface area (S_g) was calculated according to Eq. (1):

$$S_g = \frac{C}{N_{tex}} \times 10000 \quad (1)$$

where S_g is the geometric specific surface area (m^2·g^{-1}), C is the fiber cross-sectional perimeter (m), and N_{tex} is the linear density (dtex). The calculation assumes an infinitely long fiber, thereby neglecting the end-surface contributions.

Surface roughness

The surface roughness (SMD, μm) of the fabrics was measured using a KES-FB4 surface tester (Kato Tech Co., Ltd.). A probe traversed the fabric surface at a constant vertical load of 10 gf (0.098 N) and a speed of 1 mm·s^{-1}; vertical displacement was recorded in real time *via* a linear variable differential transformer (LVDT). The sample dimensions were 20 cm × 20 cm. Five measurements were performed along the warp and weft directions and were averaged. The testing environment was maintained at (20±2) °C and 65%±2% relative humidity (RH).

Gloss distribution

The angular gloss distribution of the fabric surfaces was measured using a variable-angle goniophotometer (GP-200; Murakami Color Research Laboratory). Specimens (5 × 5 cm) were fixed on the test platform and illuminated at incident angles of −15°, −30°, −45°, and −60°. The detector collected the reflected light intensity over an angular range from −90° to +90°. The sample with the highest reflectance was used to calibrate the high-voltage sensitivity parameter, ensuring that the source signal intensity remained within the optimal range (<170%). All the subsequent samples were tested under identical conditions.

Optical properties

The optical properties of the fabrics were characterized using a UV-Vis-NIR spectrophotometer (UV-3600, Shimadzu) equipped with an integrating-sphere attachment. Measurements were conducted over a wavelength range of 250–2500 nm with a scanning step of 2 nm and slit width of 20 nm using an external dual-detector configuration. A standard barium sulfate ($BaSO_4$) white reference plate was used for baseline correction prior to the measurement. The absorptance (A) was calculated from the measured total reflectance (R) as $A = 1 - R$ because the high areal density (about 245 g·m^{-2}) and dense plain-weave structure (25 ends·cm^{-1} × 17 picks·cm^{-1}) rendered the fabrics effectively opaque; the transmitted light was negligible and was not separately quantified.

Photothermal conversion performance

Photothermal conversion performance was evaluated under simulated sunlight using a xenon arc lamp at an irradiance of 600 W·m^{-2} (calibrated with a standard optical power meter). Each sample was illuminated for 10 min followed by natural cooling for 10 min. The fabric surface temperature was monitored in real-time using a multichannel temperature recorder (SH-X).

Thermal insulation performance

The thermal insulation performance was assessed using the hot-plate method. The fabric specimens were placed flat on a hot plate maintained at 37 °C and the upper surface temperature was monitored using an infrared thermal imager. After thermal equilibrium was reached, the temperature difference (ΔT) between the hot plate and upper surface of the fabric was recorded as the insulation metric. The ambient temperature was maintained at 15 °C. Five replicate measurements were performed for each sample, and the results were averaged.

Wicking behavior

Vertical wicking tests were performed to evaluate the capillary

effects on the fabrics. Specimens (25 × 3 cm) were suspended vertically with the lower end immersed in distilled water, and the water level was defined as the zero point. The wicking height was recorded over 30 min at 5 min intervals. The tests were conducted at (20±2) °C and 65%±2% relative humidity (RH). Measurements were performed in triplicate for each sample.

Dyeing performance

The fabrics were dyed with C.I. Disperse Yellow RGFL at 2.5% owf (on weight of fabric) (bath ratio 1:25) using an infrared laboratory dyeing machine. The dyebath contained 1 g·L^{-1} high-temperature leveling agent, 1 g·L^{-1} sodium lignosulfonate, and 3 g·L^{-1} methyl cinnamate as the carrier, and the pH was adjusted to 4.8–4.9 with acetic acid. The temperature was increased from 40 °C to 110 °C at 2 °C·min^{-1} and maintained at 110 °C for 60 min. After cooling, the fabrics were rinsed with hot water to remove the surface unfixed dye and air dried. The CIE *Lab** color coordinates and color difference (ΔE) of the fabrics were determined using a spectrophotometer (Datacolor 600) under the standard illuminant D65 with a 10° standard observer. Five measurements were performed for each sample and were averaged.

Mechanical properties

Tensile properties of single fibers were measured using an electronic single-fiber tensile tester (XQ-2) with a gauge length of 20 mm and a crosshead speed of 20 mm·min^{-1}. At least 30 fibers were tested for each sample. The average tensile strength and elongation at break are reported.

Thermal analysis

The thermal properties and crystallinity of the fiber samples were analyzed using a differential scanning calorimeter (DSC 250). Samples were heated from 30 °C to 200 °C at 10 °C·min^{-1} under a nitrogen atmosphere. The degree of crystallinity (X_c) was calculated using Eq. (2):

$$X_c = \frac{\Delta H_m}{\omega_{PLA} \cdot \Delta H_{100}} \times 100\% \quad (2)$$

where X_c is the crystallinity (%), ΔH_m is the melting enthalpy of the fiber (J·g^{-1}), ω_{PLA} is the weight fraction of PLA in the fiber sample (99.6%), and ΔH_{100} is the melting enthalpy of 100% crystalline PLA (93.7 J·g^{-1}).[30]

RESULTS AND DISCUSSION

Morphological Characterization of Profiled PLA/Cs$_x$WO$_3$ Fibers and Fabrics

Six PLA/Cs$_x$WO$_3$ composite fibers with distinct cross-sectional geometries (F-circular, F-hollow, F-flat, F-dumbbell, F-cruciform, and F-penta-channel) were prepared *via* melt spinning to investigate the influence of cross-sectional geometry on photothermal conversion and thermal insulation, as shown in Fig. 1. By tailoring the spinneret orifice design, the specific surface area and longitudinal surface texture of the fibers were modulated while maintaining a consistent linear density (about 3.6 dtex). The SEM images revealed that the F-circular fiber exhibited a cylindrical morphology (diameter about 25 μm) with a smooth surface and uniform curvature. The F-hollow fiber displayed a concentric annular cross-section (inner cavity of about 9 μm) with a uniform wall thickness. The F-flat fiber exhibited a flat profile (width about 50 μm, thickness about 10 μm) with a smooth surface. The F-dumbbell fiber incorporated bilateral flange protrusions relative to the flat geometry, forming a symmetrically grooved cross-section. The F-cruciform fibers possessed a four-fold symmetric arm-like structure (arm length about 10 μm, arm width about 8 μm). The F-penta-channel fiber exhibited a multi-ridge configuration with a periodically undulating surface. Geometric analysis further demonstrated that both the fiber specific surface area and the fabric surface roughness (SMD) increased monotonically with profile complexity (Table 2). For instance, the F-penta-channel fiber achieved a specific surface area of 0.4381 m^2·g^{-1}, representing a 93.7% increase over the F-circular fiber (0.2262 m^2·g^{-1}). Correspondingly, the fabric surface roughness increased from 6.4767 μm to 8.4217 μm, an increase of 30.0%. This cross-section geometry-driven surface topography evolution establishes a structural basis for tuning the optical and thermal properties.[26,27,31]

Table 2 Geometric parameters and surface properties of profiled PLA/Cs$_x$WO$_3$ fibers and fabrics.

Sample	Geometric specific surface area	Surface roughness
F-circular	0.2262	6.4767
F-hollow	–	7.06
F-flat	0.3608	7.41
F-dumbbell	0.3776	7.5117
F-cruciform	0.3481	7.215
F-penta-channel	0.4381	8.4217

Gloss Distribution of Profiled Fabrics

The angular reflectance distributions of the fabrics were measured using a variable-angle goniophotometer (GP-200) at incident angles of −15°, −30°, −45°, and −60° (Fig. 2). The F-circular fabric exhibited pronounced specular reflection; the reflected intensity was concentrated in the mirror direction symmetric to the incident angle (*e.g.*, +60° for −60° incidence), whereas the off-specular scattering remained weak. This behavior arises from the highly directional reflection of the smooth cylindrical fiber surface. The F-hollow fabric combined enhanced specular reflection with broad-angle scattering. The internal cavity introduced additional air-solid interfaces relative to the solid circular geometry, maintaining a high specular reflectance while extending the scattering component into large-angle regions. The F-flat fabric displayed strong incident-angle dependence. At −60° oblique incidence, the flat profile induced intense specular reflection concentrated in the mirror direction. At other angles, the reflectance distribution was comparatively diffuse. This indicates that the high-aspect-ratio geometry strongly modulates directional reflection under oblique illumination. The F-cruciform fabric redistributed the reflected light in multiple directions through its four-fold symmetric arm-like structure. The angular distribution broadened markedly, with the specular intensity reduced relative to the F-dumbbell fabric, and diffuse scattering was enhanced. Therefore, the increased cross-sectional complexity weakens the directionality of the reflected light. The F-dumbbell fabric exhibited a high specular reflectance and enhanced wide-angle scattering. Compared with the F-hollow fabric, it maintained a high specular peak, whereas flange protrusions induced additional scattering interfaces that extended the reflectance distribution into large-angle regions. The F-penta-channel fabric exhibited both a high specular reflectance and broad diffuse scattering. Relative to the F-cruciform fabric, the specular peak increased while the scattering intensity at large

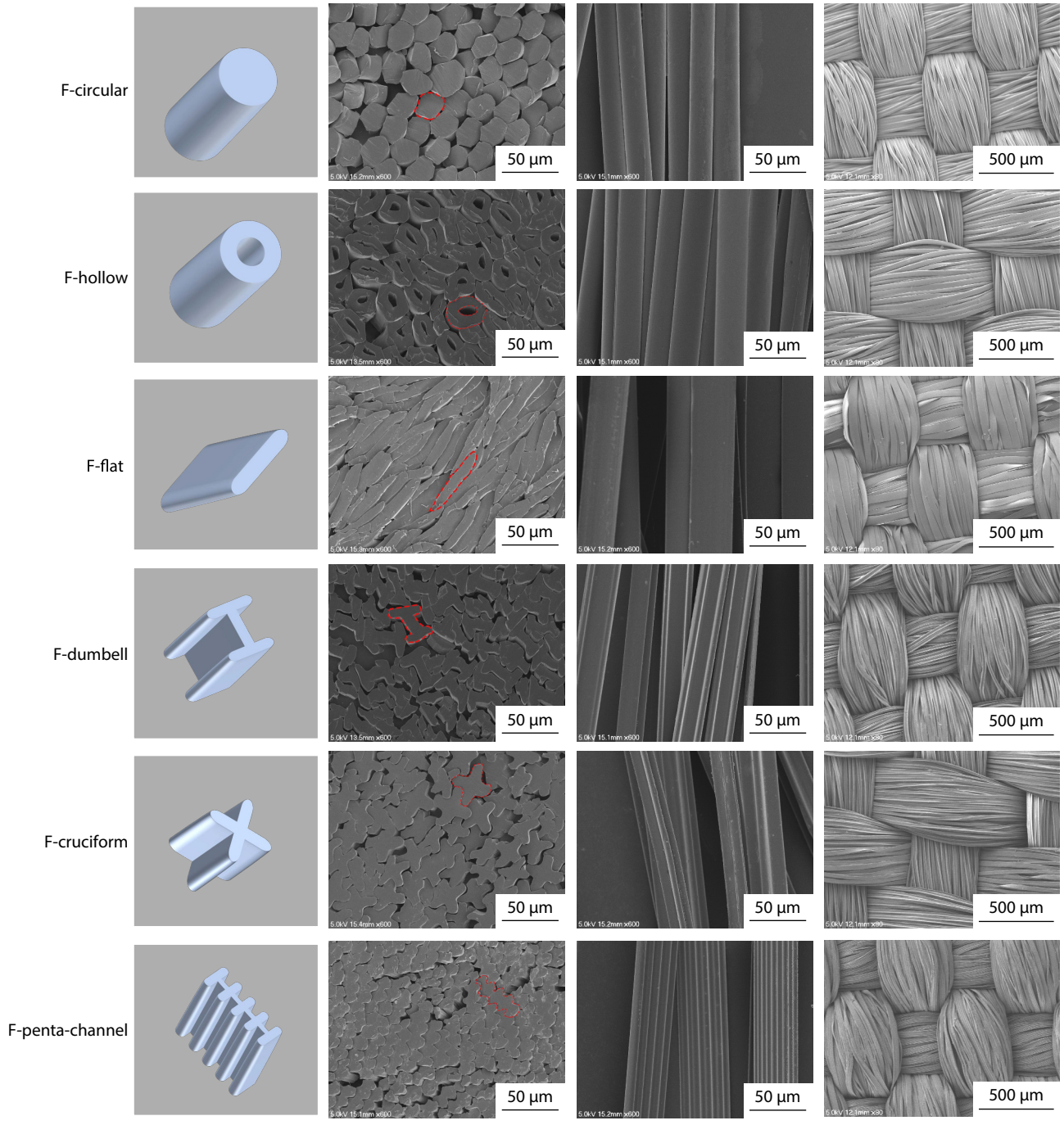


Fig. 1 SEM images of the profiled PLA/Cs_xWO_3 fibers and fabrics.

angles rose markedly, indicating that the multiridge surface structure exerts complex modulation on the optical path. These evolving gloss distribution patterns demonstrate that the cross-sectional geometry modulates the light propagation by altering the surface scattering behavior. This reconstruction of the optical path changes the visual appearance of the fabrics and establishes the structural origin of the subsequent differences in the photothermal performance.[27]

Photothermal Conversion Performance of Profiled PLA/Cs_xWO_3 Fabrics

To quantitatively elucidate the effect of the cross-sectional geometry on light absorption, the spectral absorption characteristics of the fabrics were evaluated using a UV-Vis-NIR spectrophotometer (Figs. 3a and 3b). Under controlled fabric specifications (warp and weft density, areal density, yarn twist, and twist direction), the cross-sectional morphology of the fiber substantially modulated the light absorption efficiency. The F-circular fabric exhibited the highest absorptance in the visible region (400–760 nm, 0.38–0.44) and a NIR absorptance of 0.72. As the cross-sectional complexity increased, the absorptance decreased monotonically in the following order: F-flat > F-dumbbell > F-cruciform > F-hollow > F-penta channel. The NIR ab-

https://doi.org/10.1007/s10118-026-3805-4

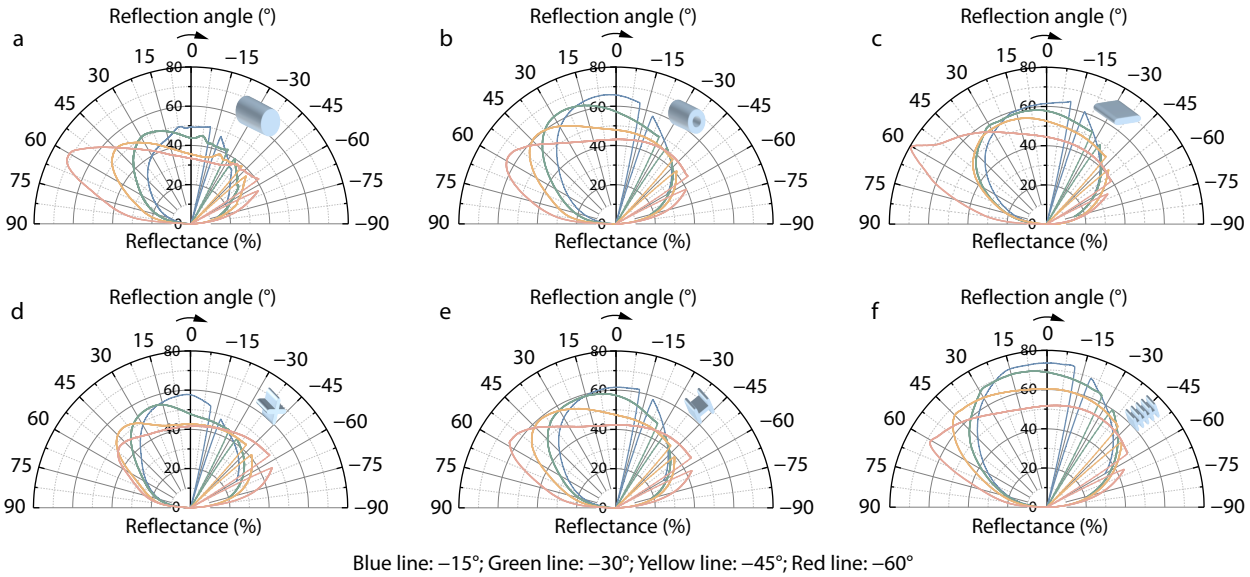


Fig. 2 Gloss distributions of the profiled PLA/Cs_xWO_3 fabrics under varying incident angles: (a) F-circular, (b) F-hollow, (c) F-flat, (d) F-dumbbell, (e) F-cruciform, and (f) F-penta-channel fabrics.

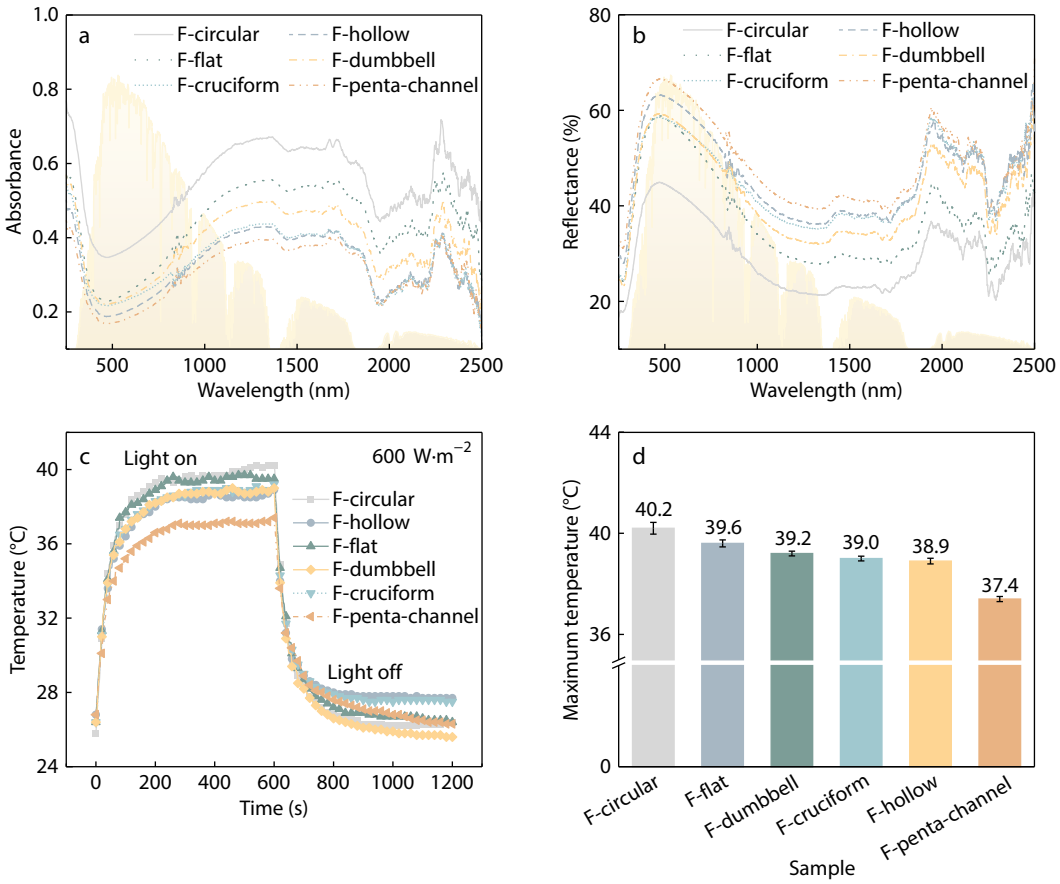


Fig. 3 Optical and photothermal properties of the profiled PLA/Cs_xWO_3 fabrics. (a) UV-Vis-NIR absorptance spectra; (b) UV-Vis-NIR reflectance spectra; (c) Photothermal heating curves under simulated solar irradiation (600 W·m^{-2}, xenon arc lamp); (d) Maximum temperature rise for the profiled PLA/Cs_xWO_3 fabrics.

sorptance of the F-penta-channel fabric is approximately 41% lower than that of the F-circular fabric.

The influence of the cross-sectional geometry on light absorption originates from the differences in the surface scattering behavior. The smooth surface of the F-circular fiber minimizes interfacial scattering losses, facilitating the penetration

of incident light into the fiber interior for absorption by Cs_xWO_3. Although the F-flat fiber possesses a flat cross section, its surface remains relatively smooth without additional protrusions; interfacial scattering losses are therefore limited, yielding an absorptance second only to that of the F-circular fabric. The F-dumbbell and F-cruciform fibers incorporate flange or arm-like protrusions that increase the scattering cross section at air-solid interfaces. A fraction of the incident light is reflected at the fiber surface rather than entering the interior, thereby shortening the effective optical path for absorption. Thus, the absorptance progressively decreases as the cross-sectional complexity increases. Despite its regular surface curvature, the F-hollow fiber contains an internal cavity that induces multiple internal reflections between the cavity wall and the fiber matrix, resulting in optical loss through photon escape. Therefore, its absorptance is between those of the F-cruciform and F-penta-channel fabrics. The multiridge surface of the F-penta-channel fiber possesses the largest specific surface area and surface roughness, producing the most pronounced interfacial scattering losses and, consequently, the lowest absorptance.

Photothermal heating tests under simulated solar irradiation (600 $W \cdot m^{-2}$, xenon arc lamp) further confirmed the correlation between spectral absorption and photothermal conversion (Figs. 3c and 3d). The F-circular fabric exhibited the optimal photothermal response, reaching a maximum temperature of 40.2 °C (temperature rise of 14.4 °C). As the cross-sectional complexity increased, the temperature rise decreased progressively, with the F-penta-channel fabric showing the lowest values (37.4 °C, temperature rise of 10.6 °C). This trend is consistent with the UV-Vis-NIR absorption spectra, demonstrating that the cross-sectional geometry governs the photothermal conversion efficiency by modulating the light-scattering behavior.[4,32]

Thermal Insulation Performance of Profiled PLA/Cs_xWO_3 Fabrics

Thermal insulation performance was evaluated using the hot-plate method (hot-plate temperature of 37 °C). The temperature difference (ΔT) between the hot plate and the fabric surface varied substantially with cross-sectional geometry (Fig. 4), following the sequence: F-cruciform (1.5 °C) > F-hollow (1.4 °C) > F-dumbbell (1.3 °C) > F-penta-channel (1.0 °C) > F-flat (0.7 °C) > F-circular (0.4 °C). This variation originates from the differences in the content and stability of the interfiber quiescent air layers.[33] The four-fold symmetric arm-like structure of the F-cruciform fiber facilitates the formation of a continuous and stable air-layer network, effectively suppressing thermal convection and conduction.[34] Although the F-hollow fiber reduces heat conduction through its enclosed air cavity, its thermal insulation is slightly inferior to that of the F-cruciform fabric, possibly because the hollow structure undergoes compression-induced deformation during weaving, compromising the stability of the trapped air layer.[34,35] The F-dumbbell and F-penta-channel fibers possess lower circumferential symmetry, resulting in less continuous inter-fiber air layers and thus exhibiting intermediate thermal insulation performance. The F-flat and F-circular fibers, owing to flat stacking and close packing, respectively, contain the lowest amount of inter-fiber quiescent air and consequently exhibit the lowest thermal resistance.[34]

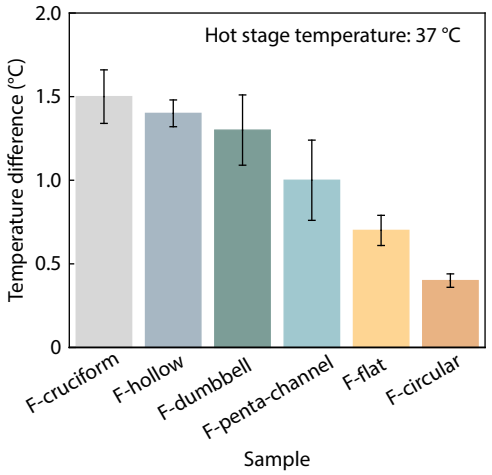


Fig. 4 Thermal insulation performance of the profiled PLA/Cs_xWO_3 fabrics.

Wicking Behavior of Profiled PLA/Cs_xWO_3 Fabrics

The wicking behavior of the fabrics was evaluated using a vertical wicking test (Fig. 5). At 30 min, the wicking heights followed the order F-cruciform (15.6 cm) > F-dumbbell (12.5 cm) > F-hollow (9.3 cm) > F-penta-channel (7.2 cm) > F-circular (6.4 cm) > F-flat (6.0 cm). This variation arises from differences in the groove structure and the resulting capillary pathways.[36] The four-fold symmetric grooves of the F-cruciform fiber establish a multidirectional capillary network, providing efficient liquid transport pathways.[37] The bilateral grooves of the F-dumbbell fiber formed effective capillary channels, giving rise to the second-highest wicking height.[36] Although the F-hollow fiber possesses an internal cavity, the inter-fiber capillary channels are limited, resulting in an intermediate wicking height. The multiridge structure of the F-penta-channel fiber increased the surface area, but the complex geometry promoted close packing of the fibers, restricting the effective capillary space. The F-circular and F-flat fibers lack pronounced groove structures; therefore, liquid transport relies primarily on surface adsorption, resulting in the lowest wicking heights.[38]

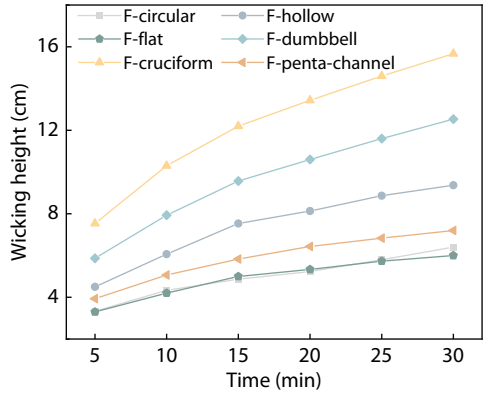


Fig. 5 Vertical wicking height of the profiled PLA/Cs_xWO_3 fabrics as a function of time.

Dyeing Performance of Profiled PLA/Cs_xWO_3 Fabrics

The colorimetric properties of the dyed fabrics (Disperse Yellow) were measured using a spectrophotometer. Macroscopic obser-

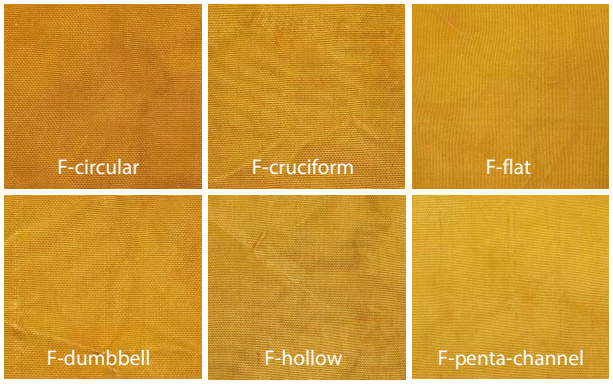


Fig. 6 Digital photographs of the dyed profiled PLA/Cs_xWO_3 fabrics.

vations (Fig. 6) revealed that the fiber cross-sectional geometry substantially influenced the apparent color depth. The F-circular fabric exhibited the deepest yellow hue, followed by that of the F-cruciform fabric. The coloration became progressively lighter as the cross-sectional complexity increased, with the F-penta-channel fabric exhibiting the lightest shade. Quantitative analysis (Fig. 7) indicated that fabric lightness (L^*) correlated positively with cross-sectional complexity, following the sequence: F-circular (L^*≈58) < F-cruciform (L^*≈64) < F-flat (L^*≈65) < F-dumbbell (L^*≈66) < F-hollow (L^*≈69) < F-penta-channel (L^*≈72). Concurrently, the b^* value (yellow–blue coordinates) decreases monotonically with increasing cross-sectional complexity. This trend originated from the enhanced surface scattering associated with the increased specific surface area (Table 2).[39,40] The enlarged specific surface area amplifies reflection losses at the fiber-air interface, reducing the effective optical path length for light–dye interactions within the fiber and manifested as increased L^* and decreased b^* values. The F-penta-channel fiber, with its multi-ridge surface, possesses the largest specific surface area (0.4381 $m^2 \cdot g^{-1}$) and surface roughness; therefore, the surface scattering losses are most pronounced, yielding the highest L^* value. The F-Circular fiber has a smooth surface (specific surface area 0.2262 $m^2 \cdot g^{-1}$); surface scattering losses are minimized, and the dye exhibits the highest light absorption efficiency, resulting in the lowest L^* and highest b^* values.

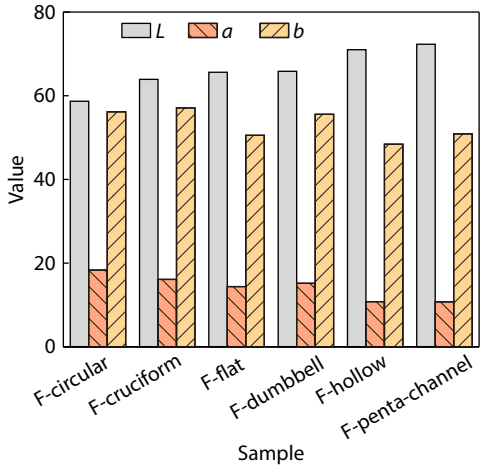


Fig. 7 CIE *Lab** color coordinates of the dyed profiled PLA/Cs_xWO_3 fabrics.

Mechanical Properties of Profiled PLA/Cs_xWO_3 Fibers

To evaluate the mechanical performance of the fibers systematically, the influence of the cross-sectional geometry on the tensile behavior was investigated under a constant linear density (Fig. 8). During profile spinning, the cross-sectional asymmetry induces a nonuniform stress field distribution.[41] Concurrently, increased surface roughness elevates the air-filament interfacial friction and resistance to internal molecular chain slippage. These factors collectively govern the crystalline orientation of a structure. However, compared with molecular-scale rearrangements, macroscopic geometric discontinuities (structural defects) dominate the mechanical performance of the profiled fibers.[41]

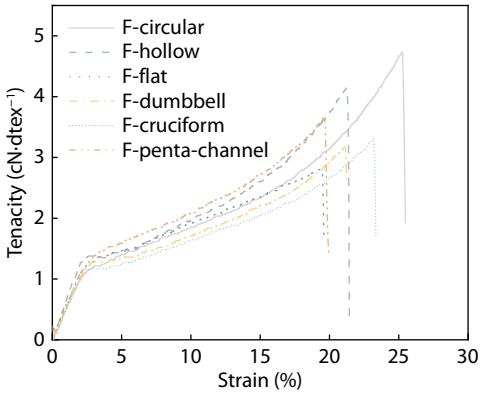


Fig. 8 Tensile stress-strain curves of the profiled PLA/Cs_xWO_3 fibers.

Cross-sectional circumferential symmetry generally benefits tensile performance, as listed in Table 3. The F-circular and F-hollow fibers achieved the highest tenacity (4.94 and 4.29 $cN \cdot dtex^{-1}$, respectively). However, despite its geometric simplicity, the F-flat fiber exhibited the lowest tenacity (3.01 $cN \cdot dtex^{-1}$) because its extreme aspect ratio (about 50 μm wide versus about 10 μm thick) created sharp-edge stress concentrators and uneven transverse cooling that generated residual thermal stress and non-uniform orientation. By contrast, the F-cruciform and F-penta-channel fibers, though more complex, achieved higher strength (3.45 and 3.73 $cN \cdot dtex^{-1}$) owing to multi-fold symmetric arms that distribute stress uniformly and suppress localized failure. Thus, the elongation at break decreased accordingly. All the profiled fibers remained processable for weaving and heat setting.

Notably, profiling conferred a higher initial modulus to the fibers (Table 3), which was closely associated with their highly oriented crystalline structure. This property provides the basis for replicating the tactile characteristics of natural fur. Additionally, the profiled fibers predominantly exhibited higher dry and wet heat shrinkage than the F-circular fibers, confirming a higher molecular chain orientation in the amorphous regions. These results elucidate the intrinsic relationship between the cross-sectional geometry and mechanical properties and establish design guidelines for practical profiled photothermal fibers.

https://doi.org/10.1007/s10118-026-3805-4

Table 3 Mechanical properties of profiled PLA/Cs_xWO_3 fibers.

Sample	Tenacity (cN·dtex^{-1})	Elongation at break (%)	Initial modulus (cN·dtex^{-1})	Dry heat shrinkage (%)	Wet heat shrinkage (%)
F-circular	4.94±0.63	26.14±2.02	46.63±4.19	12.38±0.41	13.38±0.41
F-hollow	4.29±0.72	22.77±2.01	52.48±9.62	11.33±0.49	12.52±0.57
F-penta-channel	3.73±0.93	21.75±2.51	55.16±10.29	12.00±0.29	14.56±0.53
F-cruciform	3.45±0.81	24.07±2.33	53.17±11.47	12.91±0.26	15.42±0.19
F-dumbbell	3.33±0.46	21.72±2.60	60.20±8.28	13.56±0.22	15.40±0.21
F-flat	3.01±0.80	20.09±2.21	50.60±11.75	13.36±0.29	14.47±0.22

Thermal Properties of Profiled Fibers

The influence of the cross-sectional geometry on the thermal transition behavior was investigated using differential scanning calorimetry (DSC) to evaluate the melting characteristics and crystalline perfection of the fibers (Fig. 9 and Table 4). Relative to the F-circular fiber, all profiled fibers exhibited overall increased melting temperatures (T_m) and degrees of crystallinity (X_c): T_m rose from 160.58 °C to the range of 161.28–162.50 °C, and X_c increased from 49.16% to 49.38%–51.85%. The modest fluctuation in X_c among the profiled fibers (*e.g.*, F-cruciform 49.38% versus F-dumbbell 51.47%) reflects the different intensities of the non-uniform stress fields generated by their distinct geometric asymmetries during profile spinning and hot drawing. Unlike the uniform stress distribution in the geometrically isotropic F-circular fiber, these asymmetric stress fields promote preferential molecular orientation and dense chain packing, thereby yielding more perfect crystalline structures with elevated T_m and X_c.[42,43] These results demonstrate that cross-sectional profiling is an effective strategy for enhancing the thermal stability of PLA-based fibers and broadening the heat-setting processing window.

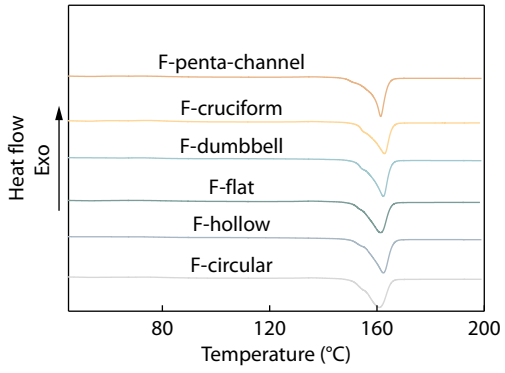


Fig. 9 DSC thermograms of the profiled PLA/Cs_xWO_3 fibers.

Table 4 Thermal properties of profiled PLA/Cs_xWO_3 fibers.

Sample	Melting temperature (°C)	Melting enthalpy (J·g^{-1})	Degree of crystallinity (%)
F-circular	160.58	45.88	49.16
F-hollow	162.27	48.39	51.85
F-flat	161.28	46.95	50.31
F-cruciform	162.50	46.08	49.38
F-dumbbell	162.45	48.03	51.47
F-penta-channel	161.71	46.32	49.63

CONCLUSIONS

Melt-spun PLA/Cs_xWO_3 fibers with engineered cross-sections balance photothermal conversion and thermal insulation through the geometric modulation of light scattering and air entrapment. The geometrically isotropic F-circular fiber achieves the highest near-infrared absorptance (0.72) and photothermal response (temperature rise of 14.4 °C) because minimal interfacial scattering preserves the optical path within the fiber interior. In contrast, increasing the cross-sectional complexity progressively reduces light harvesting; the F-penta-channel fiber shows a 41% decrease in near-infrared absorptance relative to the circular control because multiridge architectures amplify reflection losses at the fiber-air interface. Simultaneously, profiled cross-sections enhance thermal insulation by stabilizing inter-fiber quiescent air layers. The F-cruciform and F-hollow fibers achieved the highest temperature differentials (1.5 and 1.4 °C, respectively) through four-fold symmetric air networks and enclosed cavities that suppress convective and conductive heat transfer.

The shift from specular to diffuse reflection with increasing cross-sectional complexity directly alters the dyeing depth through scattering-dependent light-dye interactions. The F-cruciform fiber exhibited the highest wicking height (15.6 cm) because its four-fold symmetric grooves establish multi-directional capillary channels. Mechanical testing demonstrates a positive correlation between circumferential symmetry and tensile strength; the F-circular and F-hollow fibers achieve 4.94 and 4.29 cN·dtex^{-1}, respectively, whereas geometric discontinuities in the F-Flat fiber reduce tenacity to 3.01 cN·dtex^{-1} through stress concentration. Despite this reduction, all profiled fibers satisfied the weaving and heat-setting requirements. DSC analysis further confirmed that geometric asymmetry during spinning promoted molecular orientation and dense chain packing, yielding slightly elevated melting temperatures (161.28–162.50 °C) and crystallinities (49.38%–51.85%) relative to the circular control.

These findings establish the cross-sectional geometry as a decisive structural parameter for tuning the multifunctional performance of bio-based photothermal fibers. Near-circular or low-aspect-ratio profiles maximize active solar heating, whereas complex hollow or cross-shaped architectures favor passive insulation and moisture management. Hybrid cross-sectional designs that integrate low-profile regions for light absorption with high-complexity segments for air entrapment may offer a promising strategy for resolving the photothermal–insulation tradeoff in next-generation sustainable thermal textiles.

Conflict of Interests

The authors declare no interest conflict.

https://doi.org/10.1007/s10118-026-3805-4

Data Availability Statement

The related data of this paper is data that should not be shared, and can be obtained from the author for reasonable reasons. The author's contact information: jcyu@suda.edu.cn.

ACKNOWLEDGMENTS

This work was financially supported by the Science and Technology Guidance Project of the China Textile Industry Federation (No. 2021003) and the Key Research and Development Program of Suzhou (No. SYC2024046).

REFERENCES

1 Patti, A.; Acierno, D. Towards the sustainability of the plastic industry through biopolymers: properties and potential applications to the textiles world. *Polymers* **2022**, *14*, 692.
2 Zheng, H.; Yang, X.; Wang, C.; Xu, Y.; Chen, H.; Zhang, T.; Zheng, X. Research progress in thermal functional fibers. *Materials* **2026**, *19*, 11.
3 Guo, Z.; Sun, C.; Wang, J.; Cai, Z.; Ge, F. High-performance laminated fabric with enhanced photothermal conversion and joule heating effect for personal thermal management. *ACS Appl. Mater. Interfaces* **2021**, *13*, 8851−8862.
4 Guo, J.; Hou, C.; Zhang, J.; Guo, K.; Xin, B.; Chen, Z. Controllable fabrication and performance characterization of ultralight 3D fluffy fibrous aerogels with synergistic thermal insulation and photothermal conversion. *Colloids Surf. A Physicochem. Eng. Aspects* **2025**, *727*, 138238.
5 Rezvani Ghomi, E. R.; Khosravi, F.; Saedi Ardahaei, A. S.; Dai, Y.; Neisiany, R. E.; Foroughi, F.; Wu, M.; Das, O.; Ramakrishna, S. The life cycle assessment for polylactic acid (PLA) to make it a low-carbon material. *Polymers* **2021**, *13*, 1854.
6 Mosomi, E. K.; Olanrewaju, O. A.; Adeosun, S. O. Pivotal role of polylactide in carbon emission reduction: a comprehensive review. *Eng. Rep.* **2024**, *6*, e12909.
7 Song, L.; Zhang, Q.; Hao, Y.; Li, Y.; Chi, W.; Cong, F.; Shi, Y.; Liu, L. Z. Effect of different comonomers added to graft copolymers on the properties of PLA/PPC/PLA-*g*-GMA blends. *Polymers* **2022**,

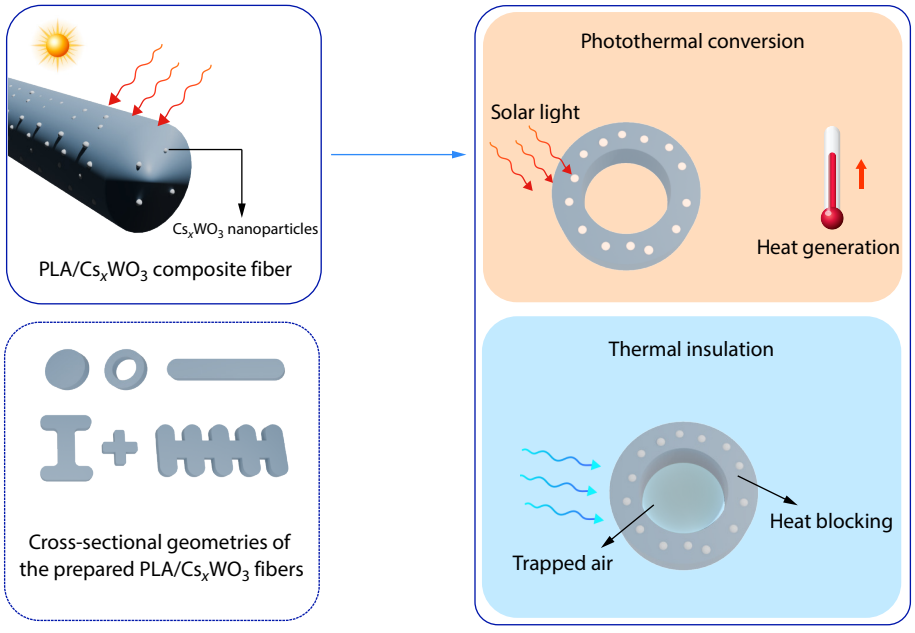
Graphical Abstract

Cross-section Engineering of Melt-spun Poly(lactic acid)/Cesium Tungsten Bronze Fibers: Balancing Photothermal Conversion and Thermal Insulation

Peng-Cheng Zheng, Jie-Rui Chen, Ji-Guang Dong, Yan-Ning Mao, Hao Huang, and Jin-Chao Yu

Soochow University

Cross-section design balances surface gloss, photothermal conversion, and thermal insulation in melt-spun poly(lactic acid) (PLA)/cesium tungsten bronze (Cs_xWO_3) fibers through modulated light scattering and air entrapment, guiding the geometric design of bio-based thermal fibers.



Chinese J. Polym. Sci. 2026 *https://doi.org/10.1007/s10118-026-3805-4*

14, 4088.
8 Ding, S.; Ma, L.; Feng, J.; Chen, Y.; Yang, D.; Wang, Q. Surface-roughness-adjustable Au nanorods with strong plasmon absorption and abundant hotspots for improved SERS and photothermal performances. *Nano Res.* **2022**, *15*, 2715–2721.
9 Adly, M. S.; Abo Kamar, S. M.; Noufal, M.; EL-Hakam, S. A.; Ahmed, A. I.; Ibrahim, A. A. A flexible photothermal device based on silver nanoparticle-integrated cellulose matrix for interfacial solar steam generation: rethink waste and reinvigorate water. *Desalination* **2026**, *617*, 119441.
10 Šišková, A. O.; Peer, P.; Andicsová, A. E.; Jordanov, I.; Rychter, P. Circulatory management of polymer waste: recycling into fine fibers and their applications. *Materials* **2021**, *14*, 4694.
11 Yu, H.; Liu, J.; Li, Z.; Jiang, X.; Jiang, L.; Xu, W. Sustainable Kapok/cotton/graphene-based textiles for thermal regulation and moisture control with innovative composite. *Ind. Crops Prod.* **2025**, *228*, 120930.
12 Lan, M.; Jia, X.; Tian, R.; Yang, J.; Shao, D.; Wang, S.; Li, Y.; Feng, L.; Song, H. Efficient green synthesis of highly concentrated and stable carbon nanotube aqueous dispersions for photothermal textile fabrication. *ACS Appl. Nano Mater.* **2022**, *5*, 8353–8361.
13 Van Pham, T.; Hirano, T.; Tanabe, E.; Septiani, E. L.; Le Anh Cao, K.; Ogi, T. Tailored nanoscale structure of flame-made antimony doped tin oxides and their near-infrared shielding properties. *Nanoscale* **2025**, *17*, 13366–13377.
14 Zhao, Y.; Ji, H.; Lu, M.; Tao, J.; Ou, Y.; Wang, Y.; Chen, Y.; Huang, Y.; Wang, J.; Mao, Y. Thermochromic smart windows assisted by photothermal nanomaterials. *Nanomaterials* **2022**, *12*, 3865.
15 Liu, J.; Ran, S.; Fan, C.; Qiao, Y.; Shi, F.; Yang, J.; Chen, B.; Liu, S. One pot synthesis of Pt-doped Cs_xWO_3 with improved near infrared shielding for energy-saving film applications. *Sol. Energy* **2019**, *178*, 17–24.
16 Li, Q.; Deng, S.; Li, D.; Yang, J.; Jin, H.; Li, J. Tungsten bronze Cs_xWO_3 nanopowders doped by Ti to enhance transparent thermal insulation ability for energy saving. *J. Alloys Compd.* **2023**, *944*, 169164.
17 Yang, J.; Tian, W.; Wang, X.; Zhao, J.; Wang, Y.; Shao, N.; Lian, L.; Huang, Q.; Ma, X. Preparation and properties of photothermal fibers by melt spinning and their durability. *J. Appl. Polym. Sci.* **2026**, *143*, e70323.
18 Zheng, P.; Liu, C.; Zhang, Y.; Bai, H.; Guan, X.; Chen, K.; Wang, H.; Xu, Y.; Yu, J. Poly (lactic acid)/cesium tungsten bronze fibers with good dyeability and high photothermal conversion performance. *ACS Appl. Polym. Mater.* **2024**, *6*, 9606–9614.
19 Ma, Y.; Tang, G. H.; Hu, Y. Modelling of hollow-fiber doping in silica aerogel composites for radiative and conductive insulation under high temperatures. *Appl. Therm. Eng.* **2024**, *254*, 123917.
20 Wang, L.; Ma, D.; Xu, C.; Gan, X.; Ge, P.; Zhu, L.; Wang, X.; Lv, Y. Preparation of flexible hollow TiO_2 fibrous membranes for thermal-insulation applications by coaxial electrospinning. *Ceram. Int.* **2023**, *49*, 22875–22881.
21 Varshney, R. K.; Kothari, V. K.; Dhamija, S. A study on thermophysiological comfort properties of fabrics in relation to constituent fibre fineness and cross-sectional shapes. *J. Text. Inst.* **2010**, *101*, 495–505.
22 He, S.; Xu, X.; Feng, P.; Yang, C.; Wang, S. Numerical simulation and experimental verification of melt-spinning parameters' effects on multi-leaf hollow-profiled fiber preparation. *Polymers* **2024**, *16*, 228.
23 Peng, Y.; Cui, Y. Thermal management with innovative fibers and textiles: manipulating heat transport, storage and conversion. *Natl. Sci. Rev.* **2024**, *11*, nwae295.
24 Spinner, M.; Kovalev, A.; Gorb, S. N.; Westhoff, G. Snake velvet black: hierarchical micro- and nanostructure enhances dark colouration in Bitis rhinoceros. *Sci. Rep.* **2013**, *3*, 1846.
25 Tao, Y.; Li, T.; Yang, C.; Wang, N.; Yan, F.; Li, L. The influence of fiber cross-section on fabric far-infrared properties. *Polymers* **2018**, *10*, 1147.
26 Liu, X.; Ning, Y.; Wang, F. Deep-black-coloring effect of fabrics made of noncircular cross-section polyester filaments. *Color Res. Appl.* **2014**, *39*, 511–518.
27 Guo, H.; Ma, B.; Yu, J.; Wang, X.; Si, Y. Photonic metafabric with biomimetic triangular light track for passive radiative cooling. *Adv. Fiber Mater.* **2025**, *7*, 106–116.
28 Knapczyk-Korczak, J.; Szewczyk, P. K.; Berniak, K.; Marzec, M. M.; Frąc, M.; Pichór, W.; Stachewicz, U. Flexible and thermally insulating porous materials utilizing hollow double-shell polymer fibers. *Adv. Sci.* **2024**, *11*, 2404154.
29 Farooq, A. S.; Zhang, P. Fundamentals, materials and strategies for personal thermal management by next-generation textiles. *Compos. Part A Appl. Sci. Manuf.* **2021**, *142*, 106249.
30 Sedlarik, V.; Kucharczyk, P.; Kasparkova, V.; Drbohlav, J.; Salakova, A.; Saha, P. Optimization of the reaction conditions and characterization of L-lactic acid direct polycondensation products catalyzed by a non-metal-based compound. *J. Appl. Polym. Sci.* **2010**, *116*, 1597–1602.
31 Karaca, E.; Ozcelik, F. Influence of the cross-sectional shape on the structure and properties of polyester fibers. *J. Appl. Polym. Sci.* **2007**, *103*, 2615–2621.
32 He, C. Y.; Zhao, P.; Zhang, H.; Chen, K.; Liu, B. H.; Lu, Z. W.; Li, Y.; La, P. Q.; Liu, G.; Gao, X. H. Efficient warming textile enhanced by a high-entropy spectrally selective nanofilm with high solar absorption. *Adv. Sci.* **2023**, *10*, e2204817.
33 Yang, F.; Wang, Z.; Zhang, W.; Wang, S.; Liu, Y. T.; Wang, F.; Surmenev, R. A.; Yu, J.; Zhang, S.; Ding, B. Superelastic and washable micro/nanofibrous sponges based on biomimetic helical fibers for efficient thermal insulation. *Nano Micro Lett.* **2025**, *18*, 42.
34 Karaca, E.; Kahraman, N.; Ömeroğlu, S.; Becerir, B. Effects of fiber cross sectional shape and weave pattern on thermal comfort properties of polyester woven fabrics. *Fibres Text. East. Eur.* **2012**, *92*, 67–72.
35 Teng, F.; Tu, L.; Wang, X.; Shen, H.; Xue, W. Ultralight air-filled hollow yarn fabrics for efficient thermal insulation and its heat and mass transfer mechanism. *Compos. Part A Appl. Sci. Manuf.* **2024**, *185*, 108281.
36 Zhang, Y.; Wang, H. P.; Chen, Y. H. Capillary effect of hydrophobic polyester fiber bundles with noncircular cross section. *J. Appl. Polym. Sci.* **2006**, *102*, 1405–1412.
37 Cui, Y.; Zhang, R.; Yu, J. Study on the liquid transport on the twisted profile filament/spun combination yarn in knitted fabric. *Polymers* **2025**, *17*, 2065.
38 Zhang, Y.; Wang, H.; Zhang, C.; Chen, Y. Modeling of capillary flow in shaped polymer fiber bundles. *J. Mater. Sci.* **2007**, *42*, 8035–8039.
39 Wei, C. A.; Li, M.; Liu, S.; Xie, D.; Li, J. Using the single-constant kubelka–munk model for surface color prediction of pre-colored fiber blends. *Coatings* **2024**, *14*, 948.
40 Tao, Y.; Zhang, S.; Xu, M.; Shu, Q.; Gao, S.; Liu, Y.; Wang, P.; Cheng, R. Preparation and application of profiled luminescent polyester fiber with reversible photochromism materials. *e-Polymers* **2024**, *24*, 20230121.
41 Takarada, W.; Ito, H.; Kikutani, T.; Okui, N. Studies on high-speed melt spinning of noncircular cross- section fibers. I. Structural analysis of as-spun fibers. *J. Appl. Polym. Sci.* **2001**, *80*, 1575–1581.
42 Qin, Q.; Zhou, T.; Wang, M.; Li, L.; Chen, N. Structure evolution and performance of poly (vinyl alcohol) fibers with controllable cross-section fabricated using a combination of melt-spinning and stretching. *Polym. Test.* **2023**, *117*, 107867.
43 Misztal-Faraj, B.; Jarecki, L.; Pęcherski, R. B. Modeling of the kinetics of polymorphic isothermal crystallization of poly (l-lactide) subjected to uniaxial molecular orientation. *Polymer* **2023**, *281*, 126126.

https://doi.org/10.1007/s10118-026-3805-4